ELSEVIER

Contents lists available at ScienceDirect

Open Ceramics

journal homepage: www.sciencedirect.com/journal/open-ceramics





CO₂ electrochemical reduction by Zn-based layered double hydroxides: The role of structural trivalent metal ions

Ryosuke Nakazato ^{a,b,*}, Keeko Matsumoto ^b, Matthias Quintelier ^c, Joke Hadermann ^c, Nataly Carolina Rosero-Navarro ^{b,d}, Akira Miura ^b, Kiyoharu Tadanaga ^{b,*}

- a National Institute of Advanced Industrial Science and Technology (AIST), Energy Process Research Institute, 16-1 Onogawa, Tsukuba, Ibaraki, 305-8569, Japan
- ^b Faculty of Engineering, Hokkaido University, Kita 13, Nishi 8, Kita-ku, Sapporo, Hokkaido, 060-8628, Japan
- ^c EMAT, Department of Physics, University of Antwerp, 2020 Antwerp, Belgium
- d Instituto de Cerámica y Vidrio, CSIC, C/Kelsen 5. Campus de Cantoblanco. 28049 Madrid, Spain

ARTICLE INFO

Keywords: CO₂ electrochemical reduction CO evolution Layered double hydroxide Zinc-based electrocatalyst Trivalent metal ion Electronic and ionic conductivity

ABSTRACT

Carbon dioxide electrochemical reduction (CO_2ER) has attracted considerable attention as a technology to recycle CO_2 into raw materials for chemicals using renewable energies. Zn-based layered double hydroxide (LDH) was recently found to be a promising CO_2ER catalyst, which is a non-precious metal catalyst with excellent selectivity for carbon monoxide (CO). However, the role of structural trivalent metal ions (M^{3+}) contained in $Zn-M^{3+}$ LDHs for the CO_2ER performance was not revealed. In this study, Zn-Cr, Zn-Ga LDHs, and Zn-Al LDHs were synthesized using a facile coprecipitation process, and their CO_2ER performance and electrochemical properties were evaluated. We found that not only Zn-Al LDH but also Zn-Cr and Zn-Ga LDHs showed CO_2ER activity for CO evolution, and the analysis by electrochemical impedance spectroscopy revealed that the type of M^{3+} in Zn-based LDHs affected their electronic and ionic conductivity, functioning as key roles for their CO_2ER performance.

1. Introduction

Global energy crisis, global warming, and environmental degradation are pressing issues, caused by increasing carbon dioxide (CO2) emissions due to the consumption of fossil resources. CO2 is an important anthropogenic greenhouse gas driving global warming, and its atmospheric concentrations have increased from approximately 278 ppm at pre-industrial levels (before 1750) to 426 ppm in 2025 [1,2]. From the perspective of carbon neutrality and energy crisis, research on technologies to convert CO2 into value-added chemical compounds has attracted attention in recent years [3,4]. CO2 conversion into value-added chemical compounds can be achieved at ambient conditions by using highly active catalysts for the CO2 reduction reaction (CO₂RR) [5]. The types of CO₂RR catalysts are classified as enzyme catalysts, photocatalysts, and electrocatalysts. Electrocatalysts have higher production rates and energy conversion efficiency than the others, which are demanded for practical applications. CO2 electrochemical reduction (CO₂ER) using electrocatalysts can make sustainable energy cycles by utilizing electricity from renewable sources such as solar and wind power [6]. CO₂ER can serve various CO₂-conversion products (carbon monoxide (CO), methane (CH₄), methanol (CH₃OH), formic acid (HCOOH), and C_{2+} products), depending on the type of electrocatalyst. Among them, CO is an important feedstock chemical for synthesizing methanol and liquid fuels [7]. Au- [8,9], Ag- [10], and Zn-based [11] electrocatalysts are known to perform highly selective CO-evolution CO_2ER , i.e., $CO_2 + H_2O + 2e^- \rightarrow CO + 2OH^-$, but Au and Ag are precious metals. From a practical point of view, electrocatalysts based on earth-abundant elements are desired [12].

In recent years, layered double hydroxide (LDH), represented by hydrotalcite, has begun to be focused as a novel CO₂ER catalyst [13]. LDH comprises positively charged metal hydroxide layers and charge-compensating anions (A^{n-}) inserted between the layers $[M_{1x}^2M^{3+}_x(OH)_2]^{x+}[A^{n-}_{x/n}]^{x-}$, which is characterized by the presence of at least two metal ions (M^{2+} and M^{3+}). Not only the diversity of metal compositions [14] but also large specific surface area [14], high hydroxide ion conductivity [15,16], and high alkaline tolerance [17,18] are favorable properties of LDH as an electrocatalyst. Although LDH has been studied for a long time as an electrocatalyst for oxygen reduction reactions [17–20] and oxygen evolution [18,19], a few research examples focus on single-phase LDH as a CO₂ER catalyst [21–25]. Among a

E-mail addresses: nakazato-ryosuke@aist.go.jp (R. Nakazato), tadanaga@eng.hokudai.ac.jp (K. Tadanaga).

https://doi.org/10.1016/j.oceram.2025.100788

^{*} Corresponding authors.

Open Ceramics 22 (2025) 100788

few examples, we reported that single-phase Ni-Al and Ni-Fe LDHs had no $\mathrm{CO}_2\mathrm{ER}$ activity, while single-phase Zn-Al LDH exhibited $\mathrm{CO}_2\mathrm{ER}$ activity for CO-evolution and that LDH was more electrochemically stable than ZnO, a typical Zn-based electrocatalyst [22]. Furthermore, it has been reported by other research groups that the CO selectivity of Zn-Al LDH can be enhanced by the introduction of third metal species such as Mg^{2+} and Ce^{3+} [24,25], resulting in nearly 90 % Faraday efficiency (*FE*) of CO evolution, indicating the high potential of Zn-based LDH as a $\mathrm{CO}_2\mathrm{ER}$ catalyst for CO evolution. However, previous studies focusing on the $\mathrm{CO}_2\mathrm{ER}$ performance of Zn-based LDH have reported only LDH with Al^{3+} as the structural trivalent metal ion. Therefore, the necessity and role of Al^{3+} have not been clarified because there are no reports focusing on the $\mathrm{CO}_2\mathrm{ER}$ performance of Zn-based LDH without Al^{3+} . What differences appear in their electrochemical properties and $\mathrm{CO}_2\mathrm{ER}$ performance between different structural trivalent metal ions (M^{3+})?

In this study, single-phase Zn-M $^{3+}$ LDHs (M $^{3+}$ = Al $^{3+}$, Cr $^{3+}$, and Ga³⁺) were synthesized by a facile coprecipitation method and the role of M³⁺ for their CO₂ER performance was investigated. Furthermore, the electrochemical impedance spectroscopy (EIS) measurements were conducted to evaluate the ionic and electronic conductivity of Zn-M³⁺ LDHs. Since conductive aids and ionomers are generally mixed with electrocatalysts to provide the electronic and ionic conduction [8,9, 21-26], high electronic and ionic conductivity of electrocatalyst itself is desirable for CO2ER. However, to the best of our knowledge, single-phase electrocatalysts with high electronic and ionic conductivity have not yet been reported for CO2ER [27]. Interestingly, LDH is reported to have different ionic conductivity, depending on their composition [28–30]. Therefore, this study is beneficial for understanding the effect of electronic and ionic conductivity of electrocatalysts on CO2ER performance. Through EIS measurements of Zn-Al and Zn-Ga LDHs, we found that the type of M³⁺ affected the electronic and ionic conductivity of Zn-based LDHs, functioning as key roles for their CO₂ER performance.

2. Experimental

2.1. Materials

R. Nakazato et al.

Zinc nitrate hexahydrate ($Zn(NO_3)_2\cdot 6H_2O$, 99.0 %), aluminium nitrate nonahydrate ($Al(NO_3)_3\cdot 9H_2O$, 98.0 %), chromium nitrate nonahydrate ($Cr(NO_3)_3\cdot 9H_2O$, 99.9 %), sodium carbonate (Na_2CO_3 , 99.8 %), potassium bicarbonate ($Na_3 > 99.5$ %), sodium hydroxide ($Na_3 > 99.5$ %), sodium hydroxide ($Na_3 > 99.5$ %), was purchased from FUJIFILM WAKO PURE CHEMICAL Co. Hydrous gallium nitrate ($Sa_3 > 99.5$ %) was purchased from KOJUNDO—CHEMICAL LABORATORY Co., Ltd. Ethanol ($Sa_3 > 99.5$ %) was purchased from KANTO CHEMICAL Co., Inc. Water was purified by a distilled water production system ($Sa_3 > 99.5$ %) was purchased from ASTOM Corp. $Sa_3 > 99.5$ %) was purchased from ASTOM Corp. $Sa_3 > 99.5$ %) was purchased from TAIYO NIPPON SANSO HOKKAIDO Corp. All other solvents and chemicals in reagent grade were purchased and were used without further purification.

2.2. Preparation of $Zn-M^{3+}$ LDH (M^{3+} = Al, Cr or Ga)

Zn-M $^{3+}$ LDHs (M $^{3+}$ = Al, Cr or Ga) were prepared using a facile and traditional coprecipitation process as shown in Fig. S1 [31,32]. For the synthesis of Zn-Al LDH with carbonate (CO $_3^{2-}$) anions, an aqueous solution containing Zn(NO $_3$) $_2\cdot$ 6H $_2$ O (62 mM) and Al(NO $_3$) $_3\cdot$ 9H $_2$ O (31 mM) with Zn $^{2+}$ /Al $^{3+}$ = 2.0 was added dropwise into a 0.15 M aqueous KHCO $_3$ solution with stirring at ambient temperature. The drop rate was adjusted to 2 mL min $^{-1}$ by using a syringe pump (SPE-1, AS ONE Corp.). The pH of the reaction mixture was adjusted to 10 by adding 2.0 M aqueous NaOH solution with a pH meter (pH700, EUTECH INSTRUMENTS Pte. Ltd.). The obtained solution was aged at 60 °C for 24 h. The resulting white precipitates were filtrated, washed with distilled water, and dried at 80 °C for 12 h. Similarly, Zn-Cr and Zn-Ga LDHs were

also prepared by replacing the controlled pH value of 10 with that of 8.5, and the Al(NO₃)₃·9H₂O with the corresponding $Cr(NO_3)_3\cdot 9H_2O$ and Ga $(NO_3)_3\cdot xH_2O$ (the approximate content of $Ga(NO_3)_3$: 59 wt%), respectively. The above controlled pH values were chosen for comparing the CO_2ER performance of single-phase LDHs because Zn-Al and Zn-Ga LDH were not obtained as a single-phase product under the pH of 8.5 and 10, respectively.

2.3. Characterization of Zn- M^{3+} LDH (M^{3+} = Al, Cr or Ga)

X-ray diffraction (XRD), scanning transmission electron microscopy coupled with energy-dispersive X-ray spectrometry (STEM-EDX), and transmission electron microscopy (TEM) were performed for characterization of the prepared samples. XRD patterns ($CuK\alpha$) were obtained using an XRD diffractometer (Mini Flex 600, RIGAKU Corp.) to identify the crystalline phase. The morphology was determined by TEM (ThermoFisher Tecnai G2 microscope operated at 200 kV and equipped with a Gatan US1000XP CCD camera). The chemical composition and distribution were determined by STEM-EDX (ThermoFisher Osiris microscope operated at 200 kV and equipped with a SuperX detector). The powder samples for TEM characterization were dissolved in ethanol and sonicated in an ultrasonic bath for 10 min before being drop-casted onto a TEM grid. ATR-IR measurements were performed with a Bruker Invenio Fourier transform spectrometer. The spectrometer is equipped with a Mercury Cadmium Telluride (MCT) cryo-detector which operates at liquid nitrogen temperature (~ 77 K). Each collected spectrum consists of an average of 32 scans (64 for the background spectrum). The ATR-IR measurements were carried out using a commercial horizontal ATR mirror unit and cell (HATR, Horizontal ATR accessory provided by Pike Technologies) equipped with an amorphous material transmitting infrared radiation (AMTIR) single crystal (internal reflection element 80×10×4 mm, 45°, Specac). Prior to the measurement, LDH samples were suspended in deionized water (~ 10 mg per 0.5 mL), deposited on the crystal and dried overnight at room temperature.

2.4. Preparation of the LDH-loaded gas diffusion electrode (GDE) as a working electrode

The LDH-loaded gas diffusion electrode (GDE) was prepared by simple drop-casting of the catalyst ink on a gas-diffusion layer (GDL: Sigracet 36BB, SGL CARBON JAPAN Ltd.). Before preparing the catalyst ink, 100 mg of each LDH sample was ground for 60 min. The catalyst ink was prepared by mixing 4 mg of the ground LDH with 1 mg of the conductive aid (carbon black: Vulcan XC72, CABOT Corp.) and 30 μL of the binder (Nafion solution, SIGMA-ALDRICH Co. LLC) in 570 μL of ethanol and sonicating for 10 min. The catalyst ink was drop-casted to the GDL on a hot plate pre-heated at 80 °C. The ink coating area was 1.89 cm² in a $\varphi 1.55$ cm round shape and the loading level of the LDH was 2.1 mg cm $^{-2}$. The LDH-loaded GDE was further dried at 80 °C for at least 30 min to remove the solvents.

2.5. CO₂ER and electrochemical impedance spectroscopy (EIS)

For Zn-M $^{3+}$ LDHs (M $^{3+}$ = Al, Cr or Ga), gas-phase CO₂ER with the LDH-loaded GDE was carried out by using a custom-made three-electrode setup composed of a three-compartment cell [23]. The cathodic and anodic compartments were separated by a piece of the anion exchange membrane to avoid the unexpected influence of the oxidation reaction taking place on the counter electrode. The LDH-loaded GDE and a platinum mesh electrode (35 × 25 mm, LAKE SHORE CRVOTRONICS Inc.) were used as working and counter electrodes, respectively. An Ag/AgCl (3.0 M KCl, BAS Inc.) electrode was used as reference. An aqueous 1.0 M KHCO₃ solution was used as catholyte and anolyte. The CO₂ gas flowed with a 50 mL min $^{-1}$ flow rate and 0.10 MPa inlet pressure to the cathodic compartment, while the solution in the

R. Nakazato et al. Open Ceramics 22 (2025) 100788

reference electrode compartment was stirred at 600 rpm with a polytetrafluoroethylene (PTFE) stirring bar. Under the above conditions, CO₂ electrolysis for 5 min was performed by applying a voltage with an electrochemical analyzer (IviumStat, IVIUM TECHNOLOGIES B.V.). Gas-phase products were detected by gas chromatography techniques (GC-2014, SHIMADZU Corp.; carrier gas: nitrogen, flow rate: 10 ml min⁻¹, pressure: 53.2 kPa, vaporization chamber temperature: 120 °C). For the detection of hydrogen (H₂), Molecular Sieve 5A (GL SCIENCES Inc.; column temperature: 50 $^{\circ}$ C, injected sample volume: 1 mL) and a thermal conductivity detector (TCD, SHIMADZU Corp.; detector temperature: 120 °C) were used. For the detection of CO and gaseous hydrocarbons, PoraPak N (GL SCIENCES Inc.; column temperature: 50 °C, injected sample volume: 1 mL) for a flame ionization detector (FID, SHIMADZU Corp.; detector temperature: 120 °C) were used. Electrode potentials in the study were converted to the reversible hydrogen electrode (RHE) or the standard hydrogen electrode (SHE) according to the following equations: $E_{\text{RHE}} = E_{\text{SHE}} + 0.059 \times \text{pH}$, $E_{\text{SHE}} = E_{\text{Ag/AgCl}} + 0.222$ V. All potentials in this work were reported after the ohmic loss correction based on EIS measurements. The FE for CO and H2 (FECO and FE_{H2} , respectively) was calculated based on the equation as follows: FE $= 2VprF(IRT)^{-1}$, where V was the volume concentration of CO or H₂ in the produced gas from the reaction cell. I was the average current (A) during the reaction, and r was the CO_2 flow rate (m³ s⁻¹) at ambient temperature and pressure. For the other constants in the formula, p was $1.013 \times 10^5 \,\mathrm{Pa}$, F was 96,485 C mol⁻¹, R was 8.3145 J mol⁻¹ K⁻¹, and T was 298 K.

For evaluating the electronic and ionic conductivity of Zn-Al and Zn-Ga LDHs, EIS measurements of the LDH-loaded GDE under the CO₂ER condition were conducted at frequencies of 10 mHz to 0.1 MHz and amplitude of 10 mV vs. the applied potential with an electrochemical analyzer (SP200, BIOLOGIC). In addition, EIS measurements of the Zn-Al and Zn-Ga LDH pellets were conducted at frequencies of 1 Hz to 7 MHz and amplitude of 100 mV vs. OCV. The LDH pellets with thickness of about 250 μm (Zn-Al: 259 μm , Zn-Ga: 242 μm) were obtained by cold pressing of 40 mg of the LDH powder with a φ 10 mm pellet press die under 300 MPa. Gold was sputtered in a φ 6 mm round shape to make electrodes on both sides of the LDH pellet with a quick coater (SC-701 Mk II, SANYU ELECTRON Co., Ltd.). The samples were kept for 24 h at 25 °C and 80 % relative humidity in constant temperature and humidity chamber (IW-221, YAMATO SCIENTIFIC Co., Ltd.) to ensure that samples reached an equilibrium, and then EIS measurement was conducted at the same condition.

3. Results and discussion

3.1. Characterization of $Zn-M^{3+}$ LDHs (M^{3+} = Al, Cr, or Ga)

Zn-M $^{3+}$ LDHs were prepared using a facile and traditional coprecipitation process, as shown in Fig. S1 [31,32]. The synthesized products were analyzed using XRD, shown in Fig. 1. The (003) and (006) plane peaks, which are characteristic of the layered structure, were observed in all samples and no impurity peaks were detected. Peaks in the Zn-Al system were assigned to the previously reported XRD pattern of Zn-Al LDH with ${\rm CO}_3^{2-}$ anions as interlayer anions [31,32]. The (003) and (006) plane peaks of the Zn-Ga and Zn-Cr systems were found to have similar diffraction angles as the Zn-Al system. This suggests that their interlayer anions are likely also carbonate anions. However, the peaks of the Zn-Cr system were broader than those of the other systems, suggesting that the primary grain size was smaller.

The TEM images in Fig. 2(a) and (b) show that the Zn-Al and Zn-Ga systems form as platelet-like crystals, a typical morphology for LDHs, with a size ranging from one hundred to several hundred nanometers. The size of the crystals in the Zn-Al and Zn-Ga systems was 50 to 550 nm and 150 to 750 nm, respectively. In addition, the rod-shaped morphology was also observed in the Zn-Al and Zn-Ga systems, as shown in Figs. S2(a) and (b), respectively. Since this shape could be

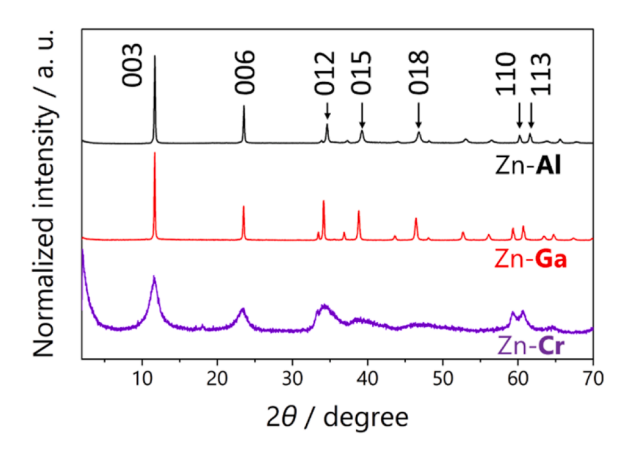


Fig. 1. XRD patterns of Zn- M^{3+} LDHs (M^{3+} = Al (black line), Ga (red line), and Cr (purple line)).

observed by looking at the particle from the parallel directions for the (001) plane of LDHs, the thickness of rod-shaped particles is indicated to be that of LDH plates. This thickness was 20 to 75 nm and 50 to 150 nm for the Zn-Al and Zn-Ga systems, respectively. On the other hand, the Zn-Cr systems exhibited unclear morphology, and the particles formed agglomerates with sizes between 50 and 400 nm, as shown in Fig. 2(c). When taking a closer look at the agglomerates, the rod-shaped morphology became apparent as shown in Fig. S2(c), indicating that the size and thickness of Zn-Cr LDH plates were 20 nm to 100 nm and 5 nm to 20 nm, respectively. STEM-EDX elemental mapping showed that Zn²⁺ and M³⁺ ions were homogeneously distributed for each system in the sub-micron-order as shown in Fig. S3. The EDX elemental analysis showed the average chemical composition with molar ratios of Zn/Al = 2.3(2), Zn/Cr = 1.99(1) and Zn/Ga = 2.15(3) for each system, which is almost the same as the starting composition ratio.

Fig. S4 shows the ATR-IR spectra of the dry LDHs. The three samples exhibited the typical spectral features of LDHs consisting of: two common broad bands in the high frequency region $(3600-2800 \text{ cm}^{-1})$ and in the low frequency region (1000-600 cm⁻¹), and an intense peak at about 1350cm⁻¹ with a weaker shoulder at slightly higher wavenumbers. The first two broad bands are due to the hydroxyl stretching vibrations of both structural M-OH species (3500-3400cm⁻¹) and molecular water present in the interlayer (3300–2950 cm⁻¹), the former, and to the superposition of the ν_2 out-of-plane stretching mode of interlayer carbonate anions ($\sim 860~\text{cm}^{-1}$) and the lattice HO-M-OH and M-OH (M = Zn, Al, Cr, or Ga) vibrational modes (450-800cm⁻¹), the latter [33]. The intense signal at around 1350 cm⁻¹ slightly asymmetric at higher wavenumbers is due to the ν_3 stretching mode of interlayer carbonate anions. While the original stretching mode of free carbonate anions is reported to be at 1415 cm⁻¹, a change in the symmetry of the molecule could lead to the splitting of v_3 into two distinct components at around 1365 cm⁻¹ and around 1415 cm⁻¹ [34]. Lastly, the other bands at 1640 cm⁻¹ and in the 1550–1480 cm⁻¹ range are attributed to the bending vibrations of the structural interlayer water molecules and physisorbed water and to the formation of surface (non-structural) carbonate-like species, due to the exposure of the material to the atmospheric CO₂, respectively.

These above results indicate that all synthesized products are LDH with the formula $[Zn_2M_1^{3^+}(OH)_6]^+$ $[CO_{0.5}^2]^-$.

3.2. CO_2ER by $Zn-M^{3+}$ LDHs (M^{3+} = Al, Cr, or Ga)

 CO_2ER by $Zn-M^{3+}$ LDHs ($M^{3+}=Al$, Cr, or Ga) was carried out with the LDH-loaded GDE and a custom-made three-electrode setup composed of a three-compartment cell [23]. The LDH-loaded GDE was prepared by simple drop-casting of the catalyst ink on a GDL. A 1.0 M aqueous KHCO $_3$ solution was used as an electrolyte. The

R. Nakazato et al. Open Ceramics 22 (2025) 100788

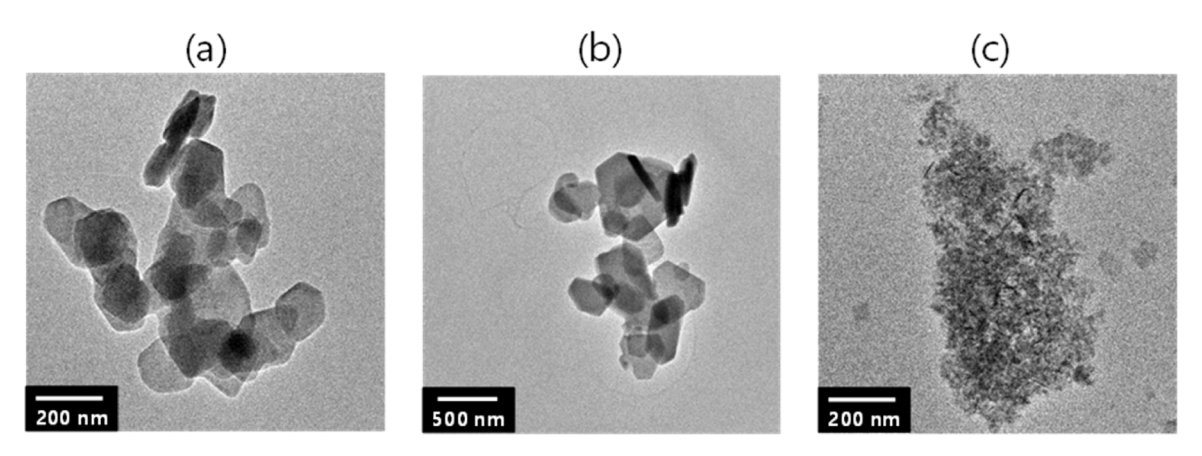


Fig. 2. TEM images of Zn-M $^{3+}$ LDHs (M $^{3+}$ = Al (a), Ga (b), and Cr (c)).

chronoamperogram of all LDHs showed an almost constant total current density (j_{total}) for 5 min of total reaction time at all the applied potentials, as shown in Fig. S5. The applied potential dependence of *FE* and *j* for the cathodic reaction are shown in Fig. 3. For all LDHs, catalytic currents associated with CO and H₂ evolution were observed, and the shortages relative to the total current could be derived from liquid products. We have reported that formic acid was detected as a minor product by CO₂ER with Zn-Al LDH as an electrocatalyst [23].

Notably, Zn-Ga LDH showed the largest partial current density of CO ($j_{\rm CO}$) and the most positive onset potential (\sim –0.48 V vs. RHE) under the relatively positive applied potential region (positive than –0.70 V vs. RHE), where the highest $FE_{\rm CO}$ s of each Zn-M³+ LDH were 63 % (at –0.61 V vs. RHE), 37 % (at –0.67 V vs. RHE), and 18 % (at –0.67 V vs. RHE) for Zn-Ga, Zn-Al, and Zn-Cr LDH, respectively. Therefore, Zn-Ga LDH was expected to have the lowest overpotential for CO evolution and to be the most active CO₂ER catalyst. However, for Zn-Ga LDH, the $j_{\rm CO}$ plateaued and the $FE_{\rm CO}$ decreased whereas the partial current density of H₂ ($j_{\rm H2}$) and $FE_{\rm H2}$ increased under the more negative applied potential region (negative than –0.70 V vs. RHE). On the contrary, Zn-Al LDH did not show the plateauing of $j_{\rm CO}$ or the decrease in $FE_{\rm CO}$ under such conditions, resulting in the highest $j_{\rm CO}$ (–14 mA cm⁻²) and $FE_{\rm CO}$ (65 %) at –0.96 V vs. RHE. For Zn-Cr LDH, the highest $FE_{\rm CO}$ of 35 % at –0.77 V vs. RHE was obtained, but $FE_{\rm CO}$ was lower than the other LDHs and H₂

evolution was dominant at all the applied potential.

3.3. Analysis for the rate-determining step (RDS) of CO_2ER based on Tafel plot

The Tafel plots afforded effective information in analyzing the factors responsible for the different catalytic activities between the three types of M^{3+} . Fig. 4 shows the Tafel plots relating to overpotential versus $j_{\rm CO}$ and $j_{\rm H2}$ for ${\rm CO_2ER}$ by Zn-M³⁺ LDHs and their Tafel slopes were summarized with typical values of FE and j in Table 1. The Tafel plots exhibited a distinct difference between the three types of M³⁺. The Tafel plots for j_{CO} showed a smaller Tafel slope for Zn-Ga LDHs (47 mV dec⁻¹) than for Zn-Al and Zn-Cr LDHs (134 and 120 mV dec⁻¹, respectively), indicating that the rate-determining step for CO₂ER (RDS_{CO2ER}) of Zn-Ga LDH was different from those of other LDHs. Figure S6 shows the proposed reaction processes of CO₂ER [35,36]. Theoretically, the Tafel slope of 118 mV dec^{-1} suggests that the RDS_{CO2ER} is the initial step of the one-electron-reduced CO_2 (CO_2^{-}) formation or the reaction step that comes before it. On the other hand, the Tafel slope of 59 mV dec⁻¹ indicates that the RDS_{CO2ER} is the reaction step that follows the initial step of the CO₂⁻ formation [36,37]. Thus, the RDS_{CO2ER} of Zn-Al and Zn-Cr LDHs is indicated to be the former while the RDS_{CO2ER} of Zn-Ga LDH is indicated to be the latter, meaning that the energy barrier of the CO₂

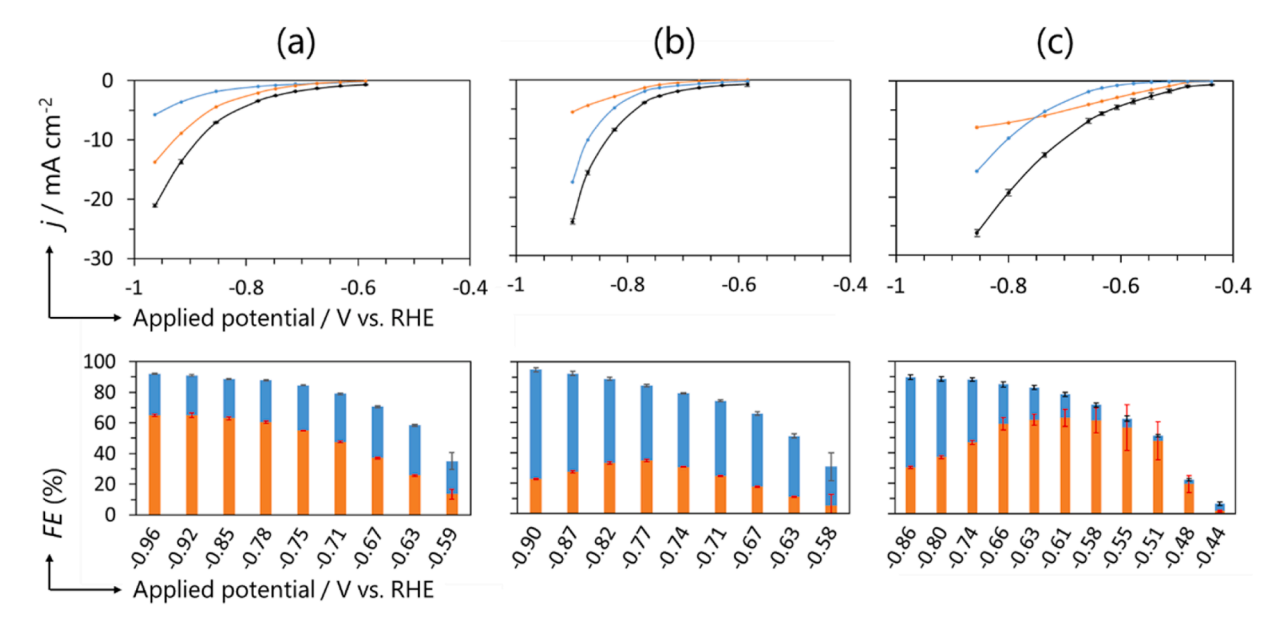


Fig. 3. Applied potential dependence of current density (j, upper row figures; black: total, orange: CO, blue: H₂) and Faradaic efficiency (FE, lower row figures; orange: CO, blue: H₂) for CO₂ER by Zn-M³⁺ LDH (M³⁺ = Al (a), Cr (b), or Ga (c)).

R. Nakazato et al. Open Ceramics 22 (2025) 100788

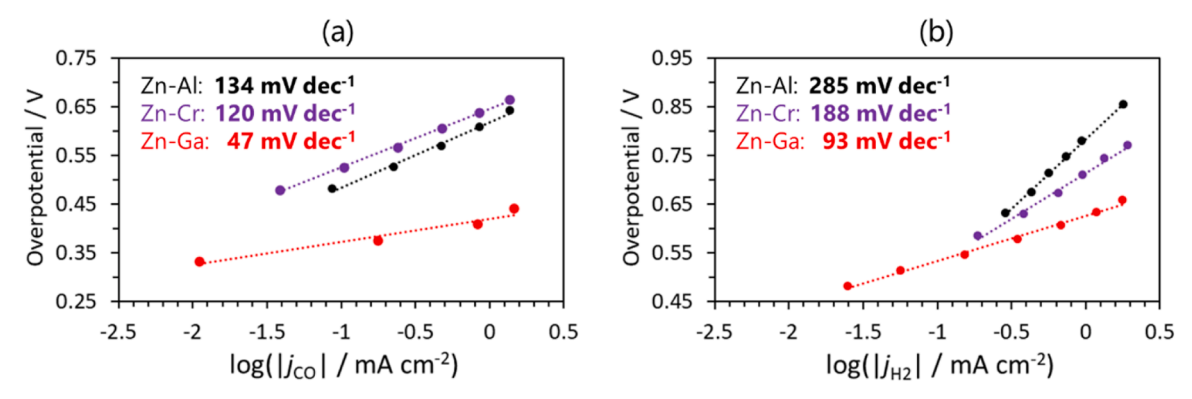


Fig. 4. Tafel plots and slopes relating to overpotential versus j_{CO} (a) and j_{H2} (b) for CO_2ER by $Zn-M^{3+}$ LDHs (M^{3+} = Al (black plots and dotted line), Cr (purple ones), or Ga (red ones)).

Table 1 Typical parameter of CO_2ER performance of $Zn-M^{3+}$ LDHs ($M^{3+}=Al$, Cr, or Ga): *FE*, *j* and Tafel slope.

Applied potential [V vs. RHE]		M ³⁺	$j_{ m total}$ [mA cm $^{-2}$]	$j_{\rm CO}$ [mA cm $^{-2}$]	j _{H2} [mA cm ⁻²]	FE _{CO} [%]	FE _{H2} [%]	Tafel slope for j_{CO} / j_{H2} [mV dec $^{-1}$]
	-0.67	Al^{3+}	-1.3	-0.48	-0.43	37	33	134 / 285
< -0.7	-0.67	Cr ³⁺	-1.4	-0.24	-0.66	18	48	120 / 188
	-0.61	Ga ³⁺	-4.5	-2.8	-0.68	63	15	47 / 93
	-0.96	Al^{3+}	-21	-14	-5.7	65	27	
> -0.7	-0.90	Cr ³⁺	-24	-5.5	-17	23	72	Same as above
	-0.86	Ga ³⁺	-26	-8.0	-15	31	59	

formation is the smallest for Zn-Ga LDH. Since the energy barrier of the CO $_2^-$ formation relates to the electron transfer onto active sites, the electronic conductivity of Zn-Ga LDH could be the highest and responsible for the smallest energy barrier and the highest performance for CO evolution under the low overpotential conditions. This hypothesis is also supported by a smaller Tafel slope for $j_{\rm H2}$ of Zn-Ga LDH (93 mV dec $^{-1}$) than that of Zn-Al and Zn-Cr LDHs (285 and 188 mV dec $^{-1}$, respectively), indicating that the high electronic conductivity of Zn-Ga LDH could also cause the promotion of H_2 evolution as well as CO evolution. On the contrary, the relatively large Tafel slope for $j_{\rm H2}$ of Zn-Al LDH indicates that the energy barrier for H_2 evolution is high, resulting in the highest performance for CO evolution under the high overpotential conditions.

3.4. Comparison of the ionic and electronic conductivity between Zn-Al and Zn-Ga LDHs

To reveal the factors responsible for the different catalytic activities between the trivalent metal ions, we evaluated the electronic and ionic conductivity of Zn-Al and Zn-Ga LDHs.

For the electronic conductivity, the difference between Zn-Al and Zn-Ga LDHs was observed from EIS measurements of the LDH-loaded GDE under the CO2ER condition. The Nyquist plots for the two LDHs under the different applied potentials are shown in Fig. S7. For both LDHs, the solution resistance (R_S) was almost constant (approximately 11 Ω), whereas the arc originating from the charge transfer resistance (RCT) was observed to be smaller as the applied potential became more negative. The $R_{\rm CT}$ of Zn-Al LDH was 42, 6.5, and 2.0 Ω at the applied potential -0.59, -0.85, and -0.96 V vs. RHE, respectively, and that of Zn-Ga LDH was 22, 3.0, and 1.5 Ω at the applied potential -0.55, -0.74, and -0.86 V vs. RHE, respectively, which was determined from the intersection of the arc with the real axis of the impedance. Although these R_{CT} were related to the H₂ evolution as well as the CO evolution, the smaller $R_{\rm CT}$ for Zn-Ga LDH than that for Zn-Al LDH indicates that the charge transfer reaction by Zn-Ga LDH was faster than that by Zn-Al LDH, resulting in the higher total current density of Zn-Ga LDH, as shown in Fig. 3. The smaller $R_{\rm CT}$ of Zn-Ga LDH could be derived from the higher electronic conductivity because a straight line with a 45° slope in front of the arcs was clearly observed for Zn-Al LDH, as shown in Fig. 5. This part can be identified as a resistance component derived from electron transfer ($R_{\rm ET}$) with approximately $4.5~\Omega$, which was determined based on the transmission line equivalent circuit model as shown in Fig. S8 [38]. Therefore, no such resistance component for Zn-Ga LDH indicates higher electronic conductivity of Zn-Ga LDH, which contributes to the smaller $R_{\rm CT}$ and Tafel slopes for $i_{\rm CO}$ and $i_{\rm H2}$.

The ionic conductivity was evaluated by EIS measurement of LDH pellets with a thickness of about 250 μ m obtained using cold pressing under 300 MPa. The Nyquist plots for Zn-Al and Zn-Ga LDHs at 25 °C and 80 % relative humidity are shown in Fig. 6. A high-frequency arc and a low-frequency tail were observed in both LDHs, but their arc sizes were different. From the values of resistance (26 and 400 k Ω for Zn-Al

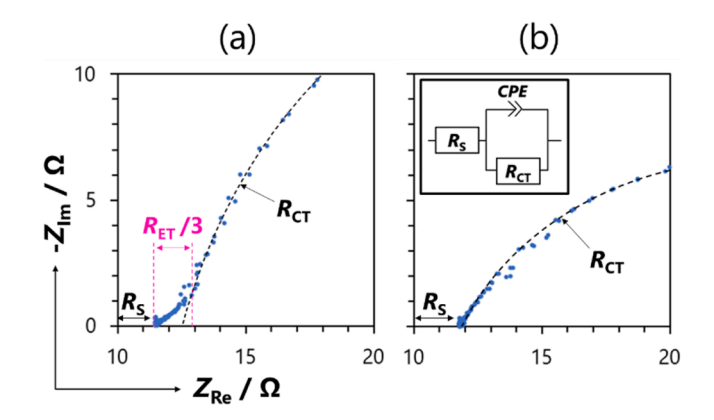


Fig. 5. Nyquist plots for the LDH-loaded GDEs under the CO_2ER at -0.59 and -0.55 V vs. RHE for Zn-Al (a) and Zn-Ga (b) LDHs, respectively. (amplitude: ± 10 mV vs. applied potential, frequency range: 1 Hz to 0.1 MHz). The inset shows the equivalent circuit for the plots of Zn-Ga LDH, where R_S was the solution resistance, R_{CT} was the charge transfer resistance, and CPE was the constant phase element. R_{ET} was the resistance component derived from electron transfer, and the equivalent circuit for the plots of Zn-Al LDH was shown in Fig. S8.

R. Nakazato et al. Open Ceramics 22 (2025) 100788

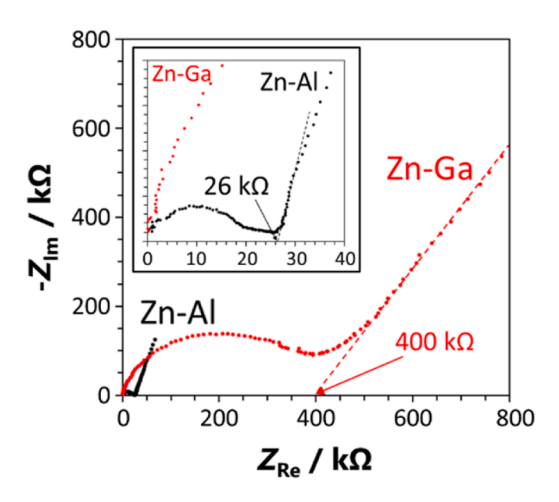


Fig. 6. Nyquist plots for the pellets of Zn-Ga (red plots) and Zn-Al (black plots) LDHs at 25 °C and 80 % relative humidity (amplitude: ± 100 mV vs. OCV, frequency range: 1 Hz to 7 MHz).

and Zn-Ga LDHs, respectively), which were determined from the intersection of the low-frequency tail with the real axis of the impedance, it was revealed that the ionic conductivity of Zn-Al LDH (3.5 µS cm⁻¹) was more than one order of magnitude higher than that of Zn-Ga LDH (0.21 μS cm⁻¹). This difference in ionic conductivity for trivalent metal ions is consistent with the previous report for Mg-Al and Mg-Ga LDHs [28]. In that study, it was reported that the difference of ion conductivity between the different proportions of trivalent metal ions could be derived from the arrangement of di- and trivalent metal ions in the (001) plane of LDH rather than interlayer space or concentration of interlayer anions. In addition, the charge carrier of LDHs has been confirmed to be hydroxide ions (OH⁻) [14,28,30]. However, the factors resulting in the difference in ionic conductivity between trivalent metal ions remain unclear. Interestingly, Figure S9 showed that the 110 reflection in Zn-Ga LDH located at a lower angle than for Zn-Al LDH, while their 003 and 006 reflections overlap, meaning that the distance between metal ions in the direction parallel to the layer is shorter in Zn-Al LDH than in Zn-Ga LDH. This shorter distance agrees with the smaller ionic radius of Al³⁺ than Ga³⁺ (Al³⁺: 0.535 Å, Ga³⁺: 0.620 Å) [39] and means that anion exchange sites is shorter in Zn-Al LDH, which may contribute to the high ionic conductivity and even the high performance for CO evolution under the high overpotential conditions. Figure S10 shows the plots of $j_{\rm CO}$ in a logarithmic scale versus applied potentials, exhibiting the curved region at the high overpotential in addition to the linear region at the low overpotential for all LDHs. The linear region corresponds to the Tafel plots as shown in Fig. 4(a), whereas the curved region is under mass transport limitation, indicating that the CO₂ER by Zn-Cr and Zn-Ga LDH contain slow mass transport steps. The lower ionic conductivity of Zn-Ga LDH than Zn-Al LDH, whose charge carriers are OH⁻, indicates that the slow reaction steps relating to OH⁻ diffusion may inhibit the CO2ER under the high overpotential condition, such as the immediate proton-coupling step and last OH desorption step in Fig. S6.

4. Conclusion

We found that not only Zn-Al LDH but also Zn-Cr and Zn-Ga LDHs showed CO₂ER activity for CO evolution. The analysis for their electrochemical properties revealed that the type of structural trivalent metal ions in Zn-based LDHs affected their electronic and ionic conductivity and functioned as key roles for their CO2ER performance as follows:

1. Al^{3+} afforded high j_{CO} and FE_{CO} under the high overpotential conditions due to the promotion of OH⁻ diffusion.

- 2. Ga^{3+} afforded high i_{CO} and FE_{CO} under the low overpotential conditions due to the promotion of electronic conductivity.
- 3. Cr³⁺ afforded low CO₂ER performance inferior to Al³⁺ and Ga³⁺

Our results suggest that high electronic conductivity and high ionic conductivity are required for designing high-performance CO2ER catalysts. This study provided helpful information for understanding the role of structural trivalent metal ions and will guide the promising design of Zn-based catalysts taken advantage of the high design flexibility of LDH for efficient energy conversion in the field of CO₂ER.

CRediT authorship contribution statement

Ryosuke Nakazato: Writing - review & editing, Writing - original draft, Visualization, Validation, Methodology, Investigation, Formal analysis, Conceptualization. Keeko Matsumoto: Investigation, Formal analysis. Matthias Quintelier: Writing - review & editing, Visualization, Investigation, Formal analysis. Joke Hadermann: Writing - review & editing, Supervision, Funding acquisition. Nataly Carolina Rosero-Navarro: Writing - review & editing, Supervision, Funding acquisition. Akira Miura: Writing - review & editing. Kiyoharu Tadanaga: Writing – review & editing, Supervision, Resources, Project administration, Funding acquisition.

Declaration of competing interest

The authors declare that they have no known competing financial interests or personal relationships that could have appeared to influence the work reported in this paper.

Acknowledgements

The authors thank Margherita Cavallo, Valentina Crocellà and Francesca Bonino for performing ATR-IR analysis. This research was supported through the 4AirCRAFT project under the strategic international cooperation between Europe (Horizon2020, No.101022633) and Japan Science and Technology Agency (JST) with reference number JPMJSC2102. 4AirCRAFT project is also supported by The Sao Paulo Research Foundation (FAPESP).

Supplementary materials

Supplementary material associated with this article can be found, in the online version, at doi:10.1016/j.oceram.2025.100788.

References

- [1] P. Friedlingstein, M. O'sullivan, M.W. Jones, R.M. Andrew, L. Gregor, J. Hauck,
 - C. Le Quéré, I.T. Luijkx, A. Olsen, G.P. Peters, W. Peters, J. Pongratz,
 - C. Schwingshackl, S. Sitch, J.G. Canadell, P. Ciais, R.B. Jackson, S.R. Alin,
 - R. Alkama, A. Arneth, V.K. Arora, N.R. Bates, M. Becker, N. Bellouin, H.C. Bittig, L. Bopp, F. Chevallier, L.P. Chini, M. Cronin, W. Evans, S. Falk, R.A. Feely,
 - T. Gasser, M. Gehlen, T. Gkritzalis, L. Gloege, G. Grassi, N. Gruber, Ö. Gürses.
 - I. Harris, M. Hefner, R.A. Houghton, G.C. Hurtt, Y. Iida, T. Ilyina, A.K. Jain,

 - A. Jersild, K. Kadono, E. Kato, D. Kennedy, K. Klein Goldewijk, J. Knauer, J. I. Korsbakken, P. Landschützer, N. Lef evre, K. Lindsay, J. Liu, Z. Liu, G. Marland,
 - N. Mayot, M.J. Mcgrath, N. Metzl, N.M. Monacci, D.R. Munro, S.I. Nakaoka,
 - Y. Niwa, K. O'brien, T. Ono, P.I. Palmer, N. Pan, D. Pierrot, K. Pocock, B. Poulter,
 - L. Resplandy, E. Robertson, C. Rodenbeck, C. Rodriguez, T.M. Rosan, J. Schwinger,
 - R. Seferian, J.D. Shutler, I. Skjelvan, T. Steinhoff, Q. Sun, A.J. Sutton, C. Sweeney,
 - S. Takao, T. Tanhua, P.P. Tans, X. Tian, H. Tian, B. Tilbrook, H. Tsujino,
 - F. Tubiello, G.R. Van Der Werf, A.P. Walker, R. Wanninkhof, C. Whitehead,
 - A. Willstrand Wranne, R. Wright, W. Yuan, C. Yue, X. Yue, S. Zaehle, J. Zeng, B. Zheng, Global carbon budget 2022, Earth Syst. Sci. Data 14 (2022) 4811–4900, https://doi.org/10.5194/ESSD-14-4811-2022
- [2] X. Lan, P. Tans, K.W. Thoning, Trends in globally-averaged CO2 determined from NOAA Global Monitoring Laboratory measurements, 2025. https://gml.noaa
- ov/ccgg/trends/global.html (accessed 17 April 2025). A. Tatin, J. Bonin, M. Robert, A. case for electrofuels, ACS Energy Lett. 1 (2016) 1062-1064, https://doi.org/10.1021/acsenergylett.6b00510
- P. De Luna, C. Hahn, D. Higgins, S.A. Jaffer, T.F. Jaramillo, E.H. Sargent, What would it take for renewably powered electrosynthesis to displace petrochemical

- processes? Science 364 (2019) eaav3506, https://doi.org/10.1126/science.
- [5] J. Qiao, Y. Liu, F. Hong, J. Zhang, A review of catalysts for the electroreduction of carbon dioxide to produce low-carbon fuels, Chem. Soc. Rev. 43 (2014) 631–675, https://doi.org/10.1039/C3CS60323G.
- [6] K. Kamiya, K. Fujii, M. Sugiyama, S. Nakanishi, CO₂ electrolysis in integrated artificial Photosynthesis systems, Chem. Lett. 50 (2021) 166–179, https://doi.org. 10.1246/cl.200691.
- [7] J.M. Spurgeon, B. Kumar, A comparative technoeconomic analysis of pathways for commercial electrochemical CO₂ reduction to liquid products, Energy Environ. Sci. 11 (2018) 1536–1551, https://doi.org/10.1039/c8ee00097b.
- [8] W.L. Zhu, R. Michalsky, O. Metin, H.F. Lv, S.J. Guo, C.J. Wright, X.L. Sun, A. A. Peterson, S.H. Sun, Monodisperse Au nanoparticles for selective electrocatalytic reduction of CO₂ to CO, J. Am. Chem. Soc. 135 (2013) 16833–16836, https://doi.org/10.1021/ja409445n.
- [9] S. Verma, Y. Hamasaki, C. Kim, W. Huang, S. Lu, H.R.M. Jhong, A.A. Gewirth, T. Fujigaya, N. Nakashima, P.J.A. Kenis, Insights into the low overpotential electroreduction of CO₂ to CO on a supported gold catalyst in an Alkaline flow electrolyzer, ACS Energy Lett. 3 (2018) 193–198, https://doi.org/10.1021/ acsenergylett.7b01096.
- [10] M. Ma, K. Liu, J. Shen, R. Kas, W.A. Smith, In situ fabrication and reactivation of highly selective and stable Ag catalysts for electrochemical CO₂ conversion, ACS Energy Lett. 3 (2018) 1301–1306, https://doi.org/10.1021/ acsenergylett.8b00472.
- [11] W. Luo, Q. Zhang, J. Zhang, E. Moioli, K. Zhao, A. Züttel, Electrochemical reconstruction of ZnO for selective reduction of CO₂ to CO, Appl. Catal. B Environ. 273 (2020) 119060, https://doi.org/10.1016/j.apcatb.2020.119060.
- [12] X. Zhang, S.-X. Guo, K.A. Gandionco, A.M. Bond, J. Zhang, Electrocatalytic carbon dioxide reduction: from fundamental principles to catalyst design, Mater. Today Adv. 7 (2020) 100074, https://doi.org/10.1016/j.mtadv.2020.100074.
- [13] C. Mousty, V. Prevot, Advances in layered double hydroxide-based materials for CO₂ electroreduction: a comprehensive review of recent research progress, Appl. Clay Sci. 253 (2024) 107362, https://doi.org/10.1016/j.clay.2024.107362.
- [14] C.I. Ezeh, M. Tomatis, X. Yang, J. He, C. Sun, Ultrasonic and hydrothermal mediated synthesis routes for functionalized Mg-Al LDH: comparison study on surface morphology, basic site strength, cyclic sorption efficiency and effectiveness, Ultrason. Sonochem. 40 (2018) 341–352, https://doi.org/10.1016/j. ultsonch.2017.07.013.
- [15] K. Tadanaga, Y. Furukawa, A. Hayashi, M. Tatsumisago, Direct ethanol fuel cell using hydrotalcite clay as a hydroxide ion conductive electrolyte, Adv. Mater. 22 (2010) 4401–4404, https://doi.org/10.1002/adma.201001766.
- [16] D. Kubo, K. Igarashi, S. Ishiyama, N.C. Rosero Navarro, A. Miura, M. Higuchi, K. Tadanaga, Enhanced hydroxide ion conductivity of Mg–Al layered double hydroxide at low humidity by intercalating dodecyl sulfate anion, J. Ceram. Soc. Japan 127 (2019) 788–792, https://doi.org/10.2109/jcersj2.19148.
- [17] H. Kowsari, M. Mehrpooya, F. Pourfayaz, Nitrogen and sulfur doped ZnAl layered double hydroxide/reduced graphene oxide as an efficient nanoelectrocatalyst for oxygen reduction reactions, Int. J. Hydrogen Energy 45 (2020) 27129–27144, https://doi.org/10.1016/j.ijhydene.2020.07.068.
- [18] L. Lu, Y. Zheng, R. Yang, A. Kakimov, X. Li, Recent advances of layered double hydroxides-based bifunctional electrocatalysts for ORR and OER, Mater. Today Chem. 21 (2021) 100488, https://doi.org/10.1016/j.mtchem.2021.100488.
- [19] Y. Arishige, D. Kubo, K. Tadanaga, A. Hayashi, M. Tatsumisago, Electrochemical oxygen separation using hydroxide ion conductive layered double hydroxides, Solid State Ionics 262 (2014) 238–240, https://doi.org/10.1016/j.ssi.2013.09.009.
- [20] Y. Iwai, A. Miura, N.C. Rosero-Navarro, M. Higuchi, K. Tadanaga, Composition, valence and oxygen reduction reaction activity of Mn-based layered double hydroxides, J. Asian Ceram. Soc. 7 (2019) 147–153, https://doi.org/10.1080/21870764.2019.1581321.
- [21] K. Iwase, T. Hirano, I. Honma, Copper aluminum layered double hydroxides with different compositions and morphologies as electrocatalysts for the carbon dioxide reduction reaction, ChemSusChem 15 (2022) e202102340, https://doi.org/ 10.1002/cssc.202102340.
- [22] N. Yamaguchi, R. Nakazato, K. Matsumoto, M. Kakesu, N.C. Rosero-Navarro, A. Miura, K. Tadanaga, Electrocatalytic property of Zn-Al layered double

- hydroxides for CO_2 electrochemical reduction, J. Asian Ceram. Soc. 11 (2023) 406–411, https://doi.org/10.1080/21870764.2023.2236441.
- [23] R. Nakazato, K. Matsumoto, N. Yamaguchi, M. Cavallo, V. Crocellà, F. Bonino, M. Quintelier, J. Hadermann, N.C.R. Navarro, A. Miura, K. Tadanaga, CO₂ electrochemical reduction with Zn-Al layered double hydroxide-loaded gas-diffusion electrode, Electrochemistry 91 (2023) 61–67, https://doi.org/10.5796/electrochemistry 23.00080
- [24] X. Ma, T. Liu, B. Lu, Y. Zhang, Synergistic effect of ZnMgAl-hydrotalcite nanomaterials electrocatalysts on high efficiency electrocatalytic reduction of CO₂ to CO, J. Alloys Compd. 973 (2024) 172858, https://doi.org/10.1016/j. iallcom.2023.172858.
- [25] F. Tan, T. Liu, E. Liu, Y. Zhang, On ZnAlCe-THs nanocomposites electrocatalysts for electrocatalytic carbon dioxide reduction to carbon monoxide, Catal. Lett. 154 (2024) 11–22, https://doi.org/10.1007/s10562-023-04302-5.
- [26] X. Du, P. Zhang, G. Zhang, H. Gao, L. Zhang, M. Zhang, T. Wang, J. Gong, Confinement of ionomer for electrocatalytic CO₂ reduction reaction via efficient mass transfer pathways, Natl. Sci. Rev. 11 (2024) nwad149, https://doi.org/ 10.1093/nsr/nwad149.
- [27] S. Hui, P. De Luna, How increasing proton and electron conduction benefits electrocatalytic CO₂ reduction, Matter Rev. 4 (2021) 1555–1577, https://doi.org/ 10.1016/j.matt.2021.02.021.
- [28] K. Miyazaki, Y. Asada, T. Fukutsuka, T. Abe, L.A. Bendersky, Structural insights into ion conduction of layered double hydroxides with various proportions of trivalent cations, J. Mater. Chem. A 1 (2013) 14569, https://doi.org/10.1039/ c3ta13632a.
- [29] D. Kubo, K. Tadanaga, A. Hayashi, M. Tatsumisago, Improvement of electrochemical performance in alkaline fuel cell by hydroxide ion conducting Ni-Al layered double hydroxide, J. Electroanal. Chem. 671 (2013) 102–105, https:// doi.org/10.1016/j.jpowsour.2012.08.093.
- [30] K. Tadanaga, Y. Furukawa, A. Hayashi, M. Tatsumisago, Effect of Mg/Al ratio on hydroxide ion conductivity for Mg-Al layered double hydroxide and application to direct ethanol fuel cells, J. Electrochem. Soc. 159 (2012) B368–B370, https://doi. org/10.1149/2.007204ies.
- [31] X. Xiong, Y. Zhao, R. Shi, W. Yin, Y. Zhao, G.I.N. Waterhouse, T. Zhang, Selective photocatalytic CO₂ reduction over Zn-based layered double hydroxides containing tri or tetravalent metals, Sci. Bull. 65 (2020) 987–994, https://doi.org/10.1016/j. scib.2020.03.032.
- [32] M. Yasaei, M. Khakbiz, A. Zamanian, E. Ghasemi, Synthesis and characterization of Zn/Al-LDH@SiO₂ nanohybrid: intercalation and release behavior of vitamin C, Mater. Sci. Eng. C 103 (2019) 109816, https://doi.org/10.1016/j. msec 2019 109816
- [33] J.T. Kloprogge, R.L. Frost, Fourier transform infrared and raman spectroscopic study of the local structure of Mg-, Ni-, and Co-hydrotalcites, J. Solid State Chem. 146 (1999) 506–515, https://doi.org/10.1006/jssc.1999.8413.
- [34] F.M. Labajos, V. Rives, M.A. Ulibarri, A ft-Ir and V-uv spectroscopic study of nickel-containing hydrotalcite-like compounds, [Ni_{1-x}Al_x(OH)₂](CO₃)_{x/2}·nH₂O, Spectrosc. Lett. 24 (1991) 499–508, https://doi.org/10.1080/00387019108018133.
- [35] M. Zhao, Y. Gu, P. Chen, Z. Xin, H. Zhu, B. Wang, K. Zhu, S. Yan, Z. Zou, Highly selective electrochemical CO₂ reduction to CO using a redox-active couple on low-crystallinity mesoporous ZnGa₂O₄ catalyst, J. Mater. Chem. A 7 (2019) 9316–9323, https://doi.org/10.1039/C9TA00562E.
- [36] G. Chen, Y. Zhao, L. Shang, G.I.N. Waterhouse, X. Kang, L. Wu, C. Tung, T. Zhang, Recent advances in the synthesis, characterization and application of Zn⁺containing heterogeneous catalysts, Adv. Sci. 3 (2016) 1500424, https://doi.org/ 10.1002/advs.201500424.
- [37] D.D. Zhu, J.L. Liu, S.Z. Qiao, Recent advances in inorganic heterogeneous electrocatalysts for reduction of carbon dioxide, Adv. Mater. 28 (2016) 3423–3452, https://doi.org/10.1002/adma.201504766.
- [38] F. Fabregat-Santiago, E.M. Barea, J. Bisquert, G.K. Mor, K. Shankar, C.A. Grimes, High carrier density and capacitance in TiO₂ nanotube arrays induced by electrochemical doping, J. Am. Chem. Soc. 130 (2008) 11312–11316, https://doi. org/10.1021/ja7108990.
- [39] R.D. Shannon, Revised effective ionic radii and systematic studies of interatomic distances in halides and chalcogenides, Acta Crystallogr. Sect. A 32 (1976) 751–767, https://doi.org/10.1107/S0567739476001551.